Generation of Nondiffracting Vector Beams with Ring-Shaped Plasmonic Metasurfaces

Yuchao Zhang, Xiaodong Yang,[*] and Jie Gao[†]

Department of Mechanical and Aerospace Engineering, Missouri University of Science and Technology, Rolla, Missouri 65409, USA

Nondiffracting Bessel, Mathieu, and Weber vector beams are generated by using ring-shaped plasmonic geometric metasurfaces. The nondiffracting vector beam is produced by the superposition of two off-axis right-handed and left-handed circularly polarized nondiffracting scalar beams described by the Whittaker integral, which are simultaneously generated by a single metasurface with the ring-shaped phase profile. The polarization states of the generated nondiffracting vector beams are analyzed by the Stokes parameters and the orbital angular momentum states are measured by the beam interference. In addition, the selfhealing properties of nondiffracting vector beams are further demonstrated, showing that not only the beam profiles but also the polarization states can be recovered behind the small opaque obstacle. The demonstrated ring-shaped plasmonic metasurfaces provide a compact and efficient platform to produce complex nondiffracting vector beams and pave the way to many promising applications related to spin and orbital angular momentum conversion, quantum information processing, optical manipulation, and optical communication.

I. INTRODUCTION

Optical vector beams with space-variant polarization states have drawn considerable interest in many areas due to their unique properties such as tight focusing, spin and orbital angular momentum, and strong longitudinal electric field [1–5]. The applications of vector beams range from optical tweezers to single molecule imaging, near-field optics, and spin-obit transformation [6–14]. Recently, vector beams combined with nondiffracting properties show the invariant transverse beam profiles and polarization states along the beam propagation under ideal conditions [15–19]. Based on the exact solution of Maxwell's equations, three types of nondiffracting scalar beams, including Bessel, Mathieu, and Weber beams, are obtained. The most common nondiffracting vector beam is the radially and azimuthally polarized Bessel vector beams, which have been proven to be useful for applications for imaging and metrology [13,14]. With selfhealing properties, it is shown that nondiffracting scalar beams could reconstruct the beam profiles after being obstructed [16,17], while for the nondiffracting vector beams with space-variant polarization states, it is essential to investigate the selfhealing properties of both the beam profiles and polarization states.

Until now, the methods used to generate nondiffracting vector beams are still limited by using the bulky spatial

light modulator (SLM) together with the complicated 4-f lens system and spatial filter for separating and combining different spin components of the vector beam. In addition, the material dispersion of SLM as well as the aberration and misalignment of optical elements greatly decrease the system's performance and limit the operational wavelength range. Recently, plasmonic metasurfaces made of nanoantenna arrays in metallic thin films have been designed for tailoring the beam wavefront. By introducing the geometric phase accompanied with polarization conversion [20–25], metasurfaces have been widely used for making integrated beam conversion devices such as optical vortex generators [26–29], flat lenses [30–35], compact wave plates [36–39], and multiplexed holograms [40–44].

Here, the ring-shaped plasmonic geometric metasurfaces are designed to produce the nondiffracting Bessel, Mathieu, and Weber vector beams across a broadband wavelength range between 500 and 1000 nm. Based on subwavelength nanoslit antenna arrays fabricated on gold films, the ring-shaped plasmonic metasurfaces with diameters of 50 μm are able to generate the nondiffracting vector beams in two separated channels by the superposition of off-axis right-handed and left-handed circularly polarized nondiffracting scalar beams described by the Whittaker integral. The polarization states of nondiffracting vector beams are analyzed by the Stokes parameters and the orbital angular momentum (OAM) states are characterized by the beam interference. Furthermore, the selfhealing properties of nondiffracting vector beams

---
[*]yangxia@mst.edu
[†]gaojie@mst.edu

are demonstrated, given that both the beam profiles and polarization states are reconstructed behind the small opaque obstacle. The designed ring-shaped plasmonic metasurfaces present a compact and effective platform for the generation of complex nondiffracting vector beams and enable a broad range of applications such as spin and orbital angular momentum conversion, quantum information processing, optical manipulation, and optical communication.

II. DESIGN OF RING-SHAPED PLASMONIC METASURFACE

The designed plasmonic metasurface consists of the subwavelength nanoslit antennas with different orientation angles etched in a gold film with a thickness of 50 nm on a glass substrate, as shown in Fig. 1(a). The nanoslit antenna has a period of 330 nm, and the width and length of each nanoslit are 60 and 200 nm, respectively. The introduced geometric phase from a nanoslit antenna is determined by the orientation angle θ of the nanoslit. When a circularly polarized beam is incident on the nanoslit antenna, the transmitted beam will contain both the original spin component with no phase shift and the converted spin component with the induced geometric phase shift of 2θ. For the right-handed circularly polarized (RCP) incidence, the transmitted left-handed circularly polarized (LCP) component has a phase shift of 2θ, while for the LCP incidence, the transmitted RCP component has a reversed phase shift

of (-2θ) [45,46]. The geometric phase of the nanoslit lies in the two plasmonic resonant modes under vertical and horizontal linear polarizations (VLP and HLP) having different phase retardations, which is similar to birefringent materials such as liquid crystals [47]. The optical field distribution and the transmission spectrum of the metasurface under circular polarization basis are simulated by employing the CST Studio Suite package, where the periodic boundary conditions are used along the x and y directions for the unit cell. The permittivity of gold is taken from spectroscopic ellipsometry data, and the refractive index of the glass substrate is 1.45. As shown in Fig. 1(b), the electric field distributions of plasmonic resonant modes for the nanoslit antenna are simulated at 1 nm above the top metal surface under different incident polarizations. It is observed that the electric field is mainly concentrated at the upper and lower edges of the nanoslit under VLP, while the electric field is concentrated at the left and right edges of the nanoslit under HLP, so that there exists strong polarization anisotropy for the nanoslit between VLP and HLP. Since the circularly polarized optical modes are the superposition of two linearly polarized modes under VLP and HLP with a $\pm\pi/2$ phase shift, the electric field distributions under RCP and LCP are mainly located at the edges of the nanoslit, but show mirror symmetry with respect to the vertical axis between them. The 50-nm-thick gold film is deposited on the glass substrate using electron-beam evaporation, then the nanoslit antenna arrays are milled in the gold film using a focused ion beam system (FEI Helios Nanolab 600, 30 kV, 9.7 pA). The SEM image of the fabricated homogeneous array of the nanoslit antenna is shown in Fig. 1(c). Figure 1(d) is the measured and simulated transmission spectra under circular polarization basis for the original spin component (LCP, green line) and the converted spin component (RCP, blue line). The transmission efficiency of plasmonic metasurfaces is relatively low due to the large Ohmic loss of metal. However, the principle of Pancharatnam-Berry (PB) geometric phase-based metasurfaces can be extended to the dielectric metasurfaces made of silicon or titanium oxide, which have very low absorption loss for manipulating light with ultrahigh transmission efficiency and high polarization conversion efficiency [23–25]. Furthermore, recently developed liquid crystal micro-optical elements based on the patterned birefringent liquid crystals can generate geometric phase profiles with very high efficiency for beam shaping [48,49]. Compared with plasmonic and dielectric metasurfaces fabricated by focused ion beam or electron-beam lithography with high costs, the liquid crystal micro-optical elements provide a competitive platform for flat optics not only with high efficiency, but also with a much lower cost.

Next, the geometric phase profiles encoded on the metasurfaces for generating the nondiffracting vector beams are derived. It has been proven that the general nondiffracting
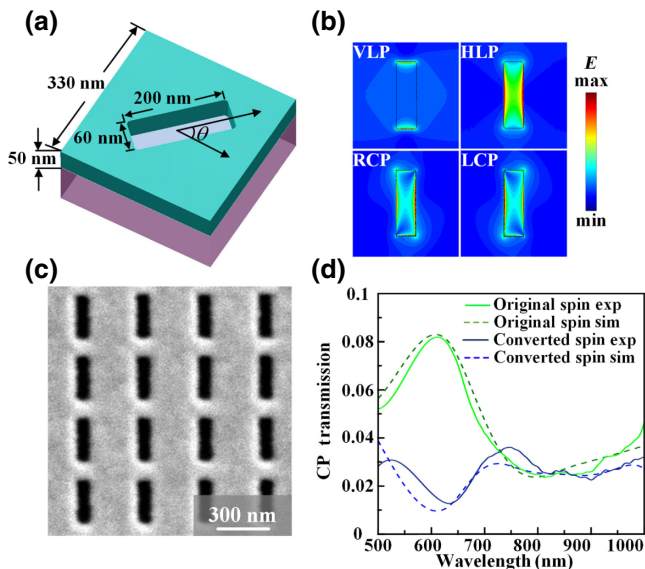

FIG. 1.   (a) Schematic of the nanoslit antenna unit cell. (b) Simulated electric field distributions of nanoslit antenna (1 nm above the top metal surface) under different incident polarizations of VLP, HLP, RCP, and LCP. (c) A SEM image of a homogeneous nanoslit array. (d) Measured and simulated transmission spectra under circular polarization basis.

scalar beam can be represented by the Whittaker integral [15,50–52]

$$\psi(r,\theta) = \frac{1}{k_t} \int_{-\pi}^{\pi} A(\varphi) \exp[ik_t r \cos(\varphi - \theta)]d\varphi. \quad (1)$$

This is the inverse Fourier transform of the function $\Psi(\rho,\varphi) = 4\pi^2 A(\varphi)\delta(\rho - k_t)/k_t\rho$ in cylindrical coordinates, and the function $A(\varphi)$ is the angular spectrum of the field $\psi(r,\theta)$ defined on a ring of radius k_t in angular spectrum space. The function $A(\varphi)$ determines the type of nondiffracting scalar beam. For the Bessel beam, $A(\varphi) = \exp(in\varphi)$. For the Mathieu beam, $A(\varphi) = ce_m(\varphi;q) + ise_m(\varphi;q)$, where $ce_m(\varphi;q)$ and $se_m(\varphi;q)$ are the even and odd angular Mathieu functions with order m and ellipticity parameter q. For the Weber beam, $A(\varphi) = \tan^{i\mu}(\varphi/2)H(\sin\varphi)/\sqrt{\sin\varphi}$, where $H(\cdot)$ is the Heaviside function [18]. After getting the function for a nondiffracting scalar beam, the form of the nondiffracting vector beam in the transverse electric (TE) mode is generated from the following process [15]

$$\mathbf{E}^{TE}(r,\theta,z) = \sqrt{2}[\psi_+(r,\theta)\mathbf{e}_- - \psi_-(r,\theta)\mathbf{e}_+]\exp(ik_z z),$$
$$(2)$$

$$\psi_\pm(r,\theta) = \int_{-\pi}^{\pi} \exp(\pm i\varphi)A(\varphi)\exp[ik_t r\cos(\varphi - \theta)]d\varphi,$$
$$(3)$$

$$\mathbf{e}_\pm = (\mathbf{e}_x \pm i\mathbf{e}_y)/\sqrt{2}, \quad (4)$$

where $\mathbf{e}_\pm$ is the circular polarization basis, $\mathbf{e}_+$ represents LCP, and $\mathbf{e}_-$ represents RCP. The function $\psi_\pm(r,\theta)$ in Eq. (3) is calculated by $\psi_\pm(r,\theta) = -i\exp(\pm i\theta)[\partial/\partial r \pm i(1/r)\partial/\partial\theta]\psi(r,\theta)$, and by substituting Eq. (1) into this equation, the function $\psi_\pm(r,\theta)$ is obtained, which is the inverse Fourier transform of the angular spectrum $\exp(\pm i\varphi)A(\varphi)$ on a ring of radius k_t.

Consequently, the nondiffracting vector beams are generated by superimposing the LCP spin component and the RCP spin component with different phase profiles on the angular spectrum plane. The phase profile for LCP is $P_L = \arg[\exp(+i\varphi)A(\varphi)]$, while the phase profile for RCP is $P_R = \arg[\exp(-i\varphi)A(\varphi)]$. Since the metasurface formed by rotating the nanoslit antennas will generate geometric phase profiles of $\varphi_{geom}(x,y)$ and $-\varphi_{geom}(x,y)$ for the LCP and RCP components, the geometric phase profiles for the LCP and RCP components need to be designed separately. In addition, in order to separate the converted spin component with respect to the original spin component, a linear phase gradient of $2\pi x/\Lambda(\Lambda = 1.6\ \mu m)$ is imposed into the phase profile so that the converted spin component will propagate off-axis with an deflection angle of $\alpha = \arctan(\lambda/\Lambda)$, where Λ is the period of the phase gradient. The geometric phase for the converted LCP spin

component is $P_L + 2\pi x/\Lambda$, while the geometric phase for the converted RCP spin component is $-(P_R + 2\pi x/\Lambda)$. Finally, the total geometric phase profile for producing the nondiffracting vector beam is obtained by superimposing the geometric phase profiles of both the LCP and RCP components and then calculating the argument of the summation complex function [46,53]. By using such an approach, the superimposed LCP and RCP components are simultaneously produced with a single metasurface, as shown in Fig. 2(a). The total geometric phase profile from the superposition of the LCP and RCP components is then expressed as

$$P_{L,R} = \arg[\exp(\pm i\varphi)A(\varphi)], \quad (5)$$

$$R_{ring} = \begin{cases} 1 & 20\ \mu m < r < 25\ \mu m \\ 0 & \text{else} \end{cases}, \quad (6)$$

$$\varphi_{geom}(x,y) = R_{ring}\ \arg\left\{\exp\left[i\left(P_L + \frac{2\pi x}{\Lambda}\right)\right]\right.$$
$$\left. + \exp\left[i\left(-P_R - \frac{2\pi x}{\Lambda}\right)\right]\right\}, \quad (7)$$

where R_{ring} is a ring function to confine the phase profile inside an annular ring since the integration of Eq. (1) to generate the nondiffracting beam is limited to an annular
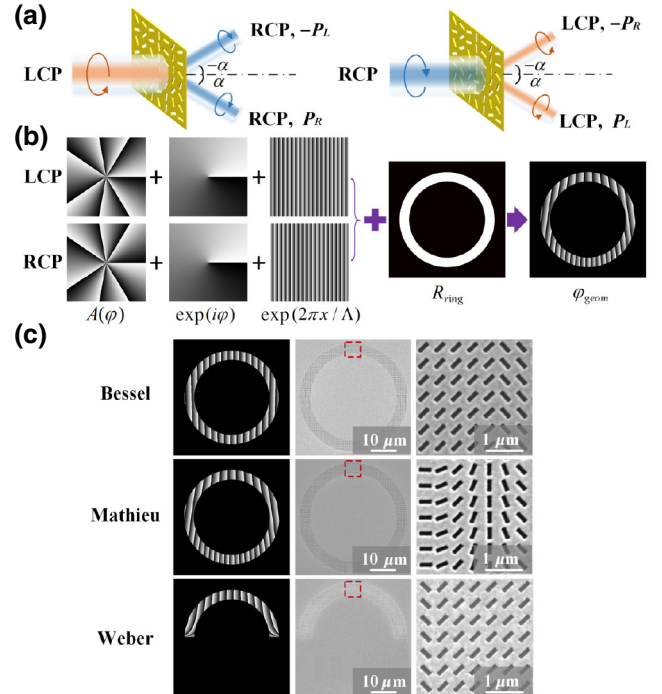

FIG. 2. (a) The converted off-axis RCP and LCP spin components transmitted from the metasurface. (b) The process for designing the total geometric phase profile encoded on the metasurface to produce the nondiffracting Mathieu vector beam. (c) Phase profiles and SEM images for the nondiffracting Bessel, Mathieu, and Weber vector beams.

ring shape in the angular spectrum plane. The total geometric phase shift $\varphi_{\mathrm{geom}}(x, y)$ defined by Eq. (7) contains two terms. For the RCP incidence, the first term with phase gradient $2\pi x/\Lambda$ will deflect the converted LCP component into the angle $\alpha = \arctan(\lambda/\Lambda)$ with the phase profile P_L, while the second term with phase gradient $-2\pi x/\Lambda$ will deflect the converted LCP component into the angle $-\alpha$ with the phase profile $-P_R$. For the RCP illumination, the situation is reversed, so that the total converted beam contains two channels at the deflection angles of α and $-\alpha$. When the input beam has linear polarization along the y axis, which is the superposition of RCP and LCP incidence as $\mathbf{e}_y = (\mathbf{e}_+ - \mathbf{e}_-)/\sqrt{2}i$, the transmitted beam is a superposition of LCP and RCP components propagated along the two deflection channels. For the channel at a deflection angle of α, the geometric phase profile is $\exp(iP_L)\mathbf{e}_- - \exp(iP_R)\mathbf{e}_+$, which matches Eqs. (2)–(4). For the channel at a deflection angle of $-\alpha$, the geometric phase profile is $\exp(-iP_R)\mathbf{e}_- - \exp(-iP_L)\mathbf{e}_+$, which also generates a nondiffracting vector beam, but the phase is inversed between LCP and RCP components compared with the first channel. Here, only the first channel is selected in the following experiment and analysis.

Figure 2(b) shows the process for designing the geometric phase profile encoded on the metasurface to generate the nondiffracting Mathieu vector beam. First, the seventh-order Mathieu function $A(\varphi) = ce_7(\varphi; q) + ise_7(\varphi, q)$ with the ellipticity parameter $q = 15$ is selected. Then the phase profiles for P_L and P_R are obtained by using Eq. (5), and the linear phase gradients $\exp(i2\pi x/\Lambda)$ and $\exp(-i2\pi x/\Lambda)$ are imposed to P_L and P_R, respectively. Finally, the total geometric phase profile for generating the nondiffracting Mathieu vector beam is obtained according to Eq. (7). With the same process, the zero-order Bessel vector beam can be generated by setting $A(\varphi) = 1$, and the fourth-order Weber vector beam is generated by setting $A(\varphi) = \tan^{i\mu}(\varphi/2)H(\sin\varphi)/\sqrt{\sin\varphi}$ with the parameter $\mu = 4$. Figure 2(c) lists the geometric phase profiles and the corresponding SEM images of the fabricated ring-shaped plasmonic metasurfaces for producing the nondiffracting Bessel, Mathieu, and Weber vector beams in the wavelength range from 500 to 1000 nm.

III. MEASUREMENT OF NONDIFFRACTING VECTOR BEAMS

Figure 3 shows the schematic of the experimental setup. The collimated optical beam from a laser diode at wavelengths of 532, 633, 808, or 988 nm is first transmitted through a linear polarizer to create the linearly polarized beam with y axis polarization, and then the input beam is focused onto the metasurface by a $10\times$ objective lens. The converted nondiffracting vector beam splits into two channels with deflection angles of $\alpha = 21°$ and $-\alpha = -21°$, and only the first channel is measured. Another $10\times$
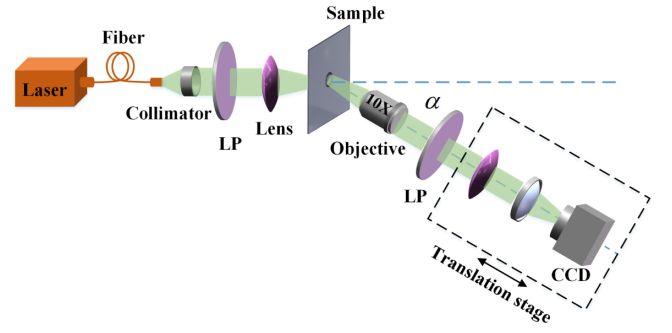

FIG. 3. Schematic of the experimental setup to measure the nondiffracting vector beam.

objective lens for the Fourier transform is placed along the deflection direction to obtain the nondiffracting vector beam.

The generated nondiffracting Bessel, Mathieu, and Weber vector beams shown in Fig. 4 are observed 10 cm behind the Fourier transform lens. The first column plots the intensity distributions of the three types of vector beams without being analyzed by the linear polarizer, and the second to fifth columns are the intensity distributions analyzed with the linear polarizer with rotation angles of $0°$, $45°$, $90°$, and $135°$. The first row shows the transverse intensity distributions of the zero-order Bessel vector beam, displaying the petal structures with a petal number of two and the azimuthal polarization. It is easy to prove that for the zero-order Bessel beam $A(\varphi) = 1$, the explicit solutions for the zero-order Bessel vector beam is $\psi_\pm(r, \theta) = 2i\pi J_1(k_t r)\exp(\pm i\theta)$ and $\mathbf{E}^{\mathrm{TE}}(r, \theta) = 4\pi J_1(k_t r)[-\sin(\theta)\mathbf{e}_x + \cos(\theta)\mathbf{e}_y]$, which represents an azimuthally polarized beam. The second row gives the transverse intensity profiles of the seventh-order Mathieu
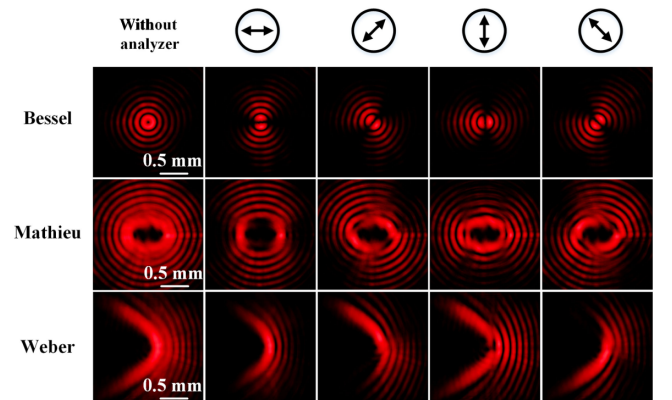

FIG. 4. The intensity distributions without polarization analyzer (the first column) and the intensity distributions analyzed with the linear polarizer with angles of $0°$, $45°$, $90°$, and $135°$ (the second to fifth columns) for the generated nondiffracting Bessel, Mathieu, and Weber vector beams 10 cm behind the Fourier transform lens at 633 nm.

vector beam, showing the patterns of elliptic rings and the petal structures with a petal number of two away from the beam center. As the linear polarizer rotates, the petal structure also rotates, which indicates the beam is nearly azimuthally polarized away from the center. For the main lobe near the beam center, the more complex polarization structure is observed and it also varies with the linear polarizer. The third row plots the transverse intensity profiles of the fourth-order Weber vector beam, giving the patterns of parabolic curves. With the linear polarizer at rotation angles of 0° and 90°, the shapes of parabolic curves are symmetric with the x axis, while at the rotation angles of 45° and 135°, the shapes of parabolic curves have nonsymmetric patterns.

Next, the polarization distributions of the nondiffracting vector beams are measured by the Stokes parameters, as shown in Fig. 5(a). The zero-order Bessel vector beam is azimuthally polarized. The polarization distribution for the seventh-order Mathieu vector beam is more complicated, where the polarization state is nearly azimuthally polarized for the zones away from the beam center, but the polarization state is close to radially polarized near the beam center. The fourth-order Weber vector beam has a similar behavior as the Mathieu vector beam, with the polarization state close to azimuthally polarized away from the beam center but radially polarized near the beam center. In order to investigate the OAM states of the nondiffracting vector beams, each generated beam is interfered with a linearly polarized plane wave through a Mach–Zehnder interferometer, and the interference patterns are shown in Fig. 5(b). The OAM state is related to the vortex structure in the beam, which can be observed as the fork structure in the interference pattern. It is shown that no vortex structure exists for the zero-order Bessel vector beam. For the seventh-order Mathieu vector beam, there are seven separated vortices with unity topological charge present within the main lobe of the beam (marked with white arrows). For the fourth-order Weber vector beam, there are a series of vortices distributed along the axis of symmetry and located at the opening to the left of the parabolic curves (marked with white arrows).

FIG. 6. The intensity distributions for the generated nondiffracting Bessel, Mathieu, and Weber vector beams at different wavelengths of 532, 633, 808, and 988 nm.

Furthermore, in Fig. 6, the broadband response of the metasurface is demonstrated at four different wavelengths of 532, 633, 808, and 988 nm. The polarization analysis of the zero-order Bessel vector beam at different wavelengths is presented in Fig. 7, which shows the same results as previously measured at the wavelength of 633 nm. It is shown that the ring-shaped plasmonic metasurfaces perform well for generating all three types of nondiffracting vector beams across the wavelength range from 500 to 1000 nm, indicating the broadband operation capabilities of the metasurface.

Finally, the selfhealing properties of the generated nondiffracting vector beams are experimentally demonstrated in Fig. 8. It is well known that the nondiffracting scalar beam exhibits structure robustness against the imposed perturbation and the beam profile will be reconstructed along the propagation. Since the nondiffracting vector beam is formed by the superimposition of two nondiffracting scalar beams, it is expected that the
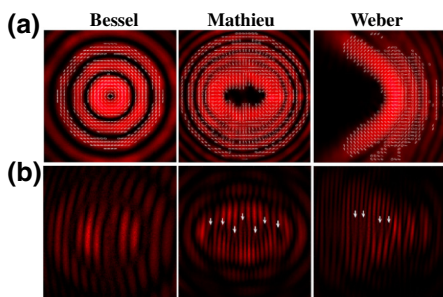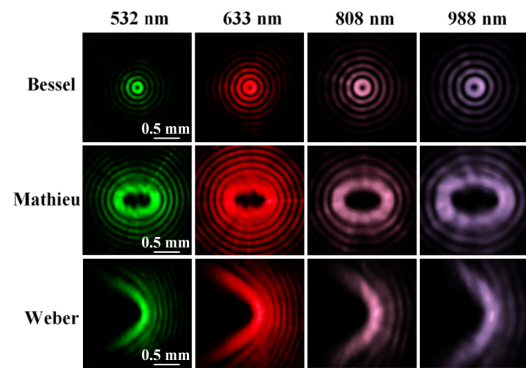

FIG. 5. Polarization distributions (a) and interference patterns (b) of the nondiffracting Bessel, Mathieu, and Weber vector beams. The vortex structures are marked by the white arrows.
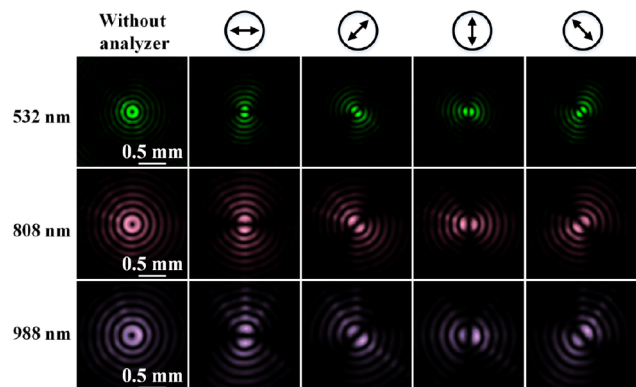

FIG. 7. The intensity distributions without the polarization analyzer (the first column) and the intensity distributions analyzed with the linear polarizer with angles of 0°, 45°, 90°, and 135° (the second to fifth columns) for the nondiffracting Bessel vector beams at different wavelengths of 532, 633, 808, and 988 nm.
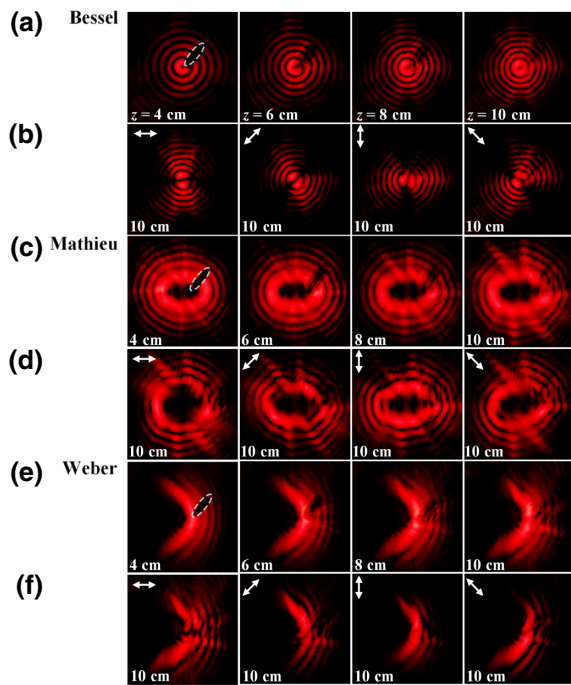
FIG. 8. (a), (c), and (e) The selfhealing processes of the non-diffracting Bessel, Mathieu, and Weber vector beams with intensity profiles plotted at $z = 4$, $z = 6$, $z = 8$, and $z = 10$ cm. (b), (d), and (f) The polarization analysis with the linear polarizer for the reconstructed beams at $z = 10$ cm.

nondiffracting vector beam is able to reconstruct both the beam profile and polarization state. A small opaque obstacle is placed at the location of $z = 4$ cm to block a part of the beam, and the beam profiles are captured at the propagation distances of $z = 6$ cm, $z = 8$ cm, and $z = 10$ cm to monitor the selfhealing properties. Figures 8(a), 8(c), and 8(e) present the reconstruction processes of the Bessel, Mathieu, and Weber vector beams, respectively. It can be seen that the blocked parts of all three types of the nondiffracting vector beams gradually recover themselves with the increasing propagation distance. At $z = 10$ cm, all the nondiffracting vector beams can completely reconstruct the blocked parts. Figures 8(b), 8(d), and 8(f) are the polarization analyses for the reconstructed beams located at $z = 10$ cm. It shows that the polarization states of the reconstructed beams have similar behaviors as those of the unperturbed beams in Fig. 4. It is demonstrated that the nondiffracting vector beams generated by the metasurfaces have the special selfhealing propagation properties where both the beam profiles and polarization states can be recovered behind the obstruction.

IV. CONCLUSION

In summary, three types of nondiffracting vector beams including Bessel, Mathieu, and Weber vector beams are generated by using the ring-shaped plasmonic geometric

metasurfaces in a broadband wavelength range from 500 to 1000 nm. The nondiffracting vector beam is produced by the superposition of two off-axis RCP and LCP nondiffracting scalar beams described by the Whittaker integral. All three types of nondiffracting vector beams are generated by the geometric phase profiles in the angular spectrum plane encoded on the ring-shaped metasurfaces. The polarization states and OAM states of the generated nondiffracting vector beams are also analyzed. The selfhealing properties of nondiffracting vector beams are further demonstrated, showing that not only the beam profiles but also the polarization states can be reconstructed behind the obstruction. The produced nondiffracting vector beams with ring-shaped plasmonic metasurfaces will advance many promising applications in spin-to-orbital angular momentum conversion, quantum information processing, particle manipulation and transportation, and optical communication.

[1] R. Dorn, S. Quabis, and G. Leuchs, Sharper Focus for a Radially Polarized Light Beam, Phys. Rev. Lett. **91**, 233901 (2003).
[2] H. Wang, L. Shi, B. Lukyanchuk, C. Sheppard, and C. T. Chong, Creation of a needle of longitudinally polarized light in vacuum using binary optics, Nat. Photonics **2**, 501 (2008).
[3] Q. Zhan and J. Leger, Focus shaping using cylindrical vector beams, Opt. Express **10**, 324 (2002).
[4] M. Padgett and R. Bowman, Tweezers with a twist, Nat. Photonics **5**, 343 (2011).
[5] Q. Zhan, Trapping metallic Rayleigh particles with radial polarization, Opt. Express **12**, 3377 (2004).
[6] R. P. Lopez, U. Ruiz, V. Arrizon, and R. R. Garcia, Optical manipulation using optimal annular vortices, Opt. Lett. **41**, 4138 (2016).
[7] L. Marrucci, E. Karimi, S. Slussarenko, B. Piccirillo, E. Santamato, E. Nagali, and F. Sciarrino, Spin-to-orbital conversion of the angular momentum of light and its classical and quantum applications, J. Opt. **13**, 064001 (2011).
[8] E. Nagali, F. Sciarrino, F. De Martini, L. Marrucci, B. Piccirillo, E. Karimi, and E. Santamato, Quantum Information Transfer from Spin to Orbital Angular Momentum of Photons, Phys. Rev. Lett. **103**, 013601 (2009).
[9] D. Naidoo, F. S. Roux, A. Dudley, I. Litvin, B. Piccirillo, L. Marrucci, and A. Forbes, Controlled generation of higher-order Poincaré sphere beams from a laser, Nat. Photonics **10**, 327 (2016).

[10] S. Segawa, Y. Kozawa, and S. Sato, Resolution enhancement of confocal microscopy by subtraction method with vector beams, Opt. Lett. **39**, 3118 (2014).

[11] E. Karimi, J. Leach, S. Slussarenko, B. Piccirillo, L. Marrucci, L. Chen, W. She, S. Franke-Arnold, M. J. Padgett, and E. Santamato, Spin-orbit hybrid entanglement of photons and quantum contextuality, Phys. Rev. A **82**, 022115 (2010).

[12] Y. Xue, C. Kuang, S. Li, Z. Gu, and X. Liu, Sharper fluorescent super-resolution spot generated by azimuthally polarized beam in STED microscopy, Opt. Express **20**, 17653 (2012).

[13] M. P. Lavery, F. C. Speirits, S. M. Barnett, and M. J. Padgett, Detection of a spinning object using light's orbital angular momentum, Science **341**, 537 (2013).

[14] V. D'Ambrosio, N. Spagnolo, L. Del Re, S. Slussarenko, Y. Li, L. C. Kwek, L. Marrucci, S. P. Walborn, L. Aolita, and F. Sciarrino, Photonic polarization gears for ultra-sensitive angular measurements, Nat. Commun. **4**, 2432 (2013).

[15] G. Méndez, A. Fernandez-Vazquez, and R. P. López, Orbital angular momentum and highly efficient holographic generation of nondiffractive TE and TM vector beams, Opt. Commun. **334**, 174 (2015).

[16] H. Li and J. Yin, Generation of a vectorial Mathieu-like hollow beam with a periodically rotated polarization property, Opt. Lett. **36**, 1755 (2011).

[17] M. A. Bandres and B. M. Rodríguez-Lara, Nondiffracting accelerating waves: Weber waves and parabolic momentum, New J. Phys. **15**, 013054 (2013).

[18] P. Zhang, Y. Hu, T. Li, D. Cannan, X. Yin, R. Morandotti, Z. Chen, and X. Zhang, Nonparaxial Mathieu and Weber Accelerating Beams. Phys. Rev. Lett. **109**, 193901 (2012).

[19] G. Wu, F. Wang, and Y. Cai, Generation and self-healing of a radially polarized Bessel-Gauss beam, Phys. Rev. A **89**, 043807 (2014).

[20] A. V. Kildishev, A. Boltasseva, and V. M. Shalaev, Planar photonics with metasurfaces, Science **339**, 1232009 (2013).

[21] M. Jang, Y. Horie, A. Shibukawa, J. Brake, Y. Liu, S. M. Kamali, A. Arbabi, H. Ruan, A. Faraon, and C. Yang, Wavefront shaping with disorder-engineered metasurfaces, Nat. Photonics **12**, 84 (2018).

[22] N. Yu and F. Capasso, Flat optics with designer metasurfaces, Nat. Mater. **13**, 139 (2014).

[23] M. Khorasaninejad, W. T. Chen, R. C. Devlin, J. Oh, A. Y. Zhu, and F. Capasso, Metalenses at visible wavelengths: Diffraction-limited focusing and subwavelength resolution imaging, Science **352**, 1190 (2016).

[24] K. Ou, G. Li, T. Li, H. Yang, F. Yu, J. Chen, Z. Zhao, G. Cao, X. Chen, and W. Lu, High efficiency focusing vortex generation and detection with polarization-insensitive dielectric metasurfaces, Nanoscale **10**, 19154 (2018).

[25] D. Lin, P. Fan, E. Hasman, and M. L. Brongersma, Dielectric gradient metasurface optical elements, Science **345**, 298 (2014).

[26] Y. Liu, Y. Ke, J. Zhou, Y. Liu, H. Luo, S. Wen, and D. Fan, Generation of perfect vortex and vector beams based on Pancharatnam-Berry phase elements, Sci. Rep. **7**, 44096 (2017).

[27] F. Yue, D. Wen, J. Xin, B. D. Gerardot, J. Li, and X. Chen, Vector vortex beam generation with a single plasmonic metasurface, ACS Photonics **3**, 1558 (2016).

[28] J. Zeng, L. Li, X. Yang, and J. Gao, Generating and separating twisted light by gradient–rotation split-ring antenna metasurfaces, Nano Lett. **16**, 3101 (2016).

[29] J. Zeng, T. S. Luk, J. Gao, and X. Yang, Spiraling light with magnetic metamaterial quarter-wave turbines, Sci. Rep. **7**, 11824 (2017).

[30] K. Zhang, X. Ding, L. Zhang, and Q. Wu, Anomalous three-dimensional refraction in the microwave region by ultra-thin high efficiency metalens with phase discontinuities in orthogonal directions, New J. Phys. **16**, 103020 (2014).

[31] K. Zhang, Y. Yuan, D. Zhang, X. Ding, B. Ratni, S. N. Burokur, M. Lu, K. Tang, and Q. Wu, Phase-engineered metalenses to generate converging and non-diffractive vortex beam carrying orbital angular momentum in microwave region, Opt. Express **26**, 1351 (2018).

[32] X. Ni, S. Ishii, A. V. Kildishev, and V. M. Shalaev, Ultrathin, planar, babinet-inverted plasmonic metalenses, Light: Sci. Appl. **2**, e72 (2013).

[33] X. Chen, L. Huang, H. Mühlenbernd, G. Li, B. Bai, Q. Tan, G. Jin, C. Qiu, S. Zhang, and T. Zentgraf, Dual-polarity plasmonic metalens for visible light, Nat. Commun. **3**, 1198 (2012).

[34] M. Khorasaninejad, W. T. Chen, A. Y. Zhu, J. Oh, R. C. Devlin, D. Rousso, and F. Capasso, Multispectral chiral imaging with a metalens, Nano Lett. **16**, 4595 (2016).

[35] F. Aieta, P. Geneve, M. A. Kats, N. Yu, R. Blanchard, Z. Gaburro, and F. Capasso, Aberration-free ultrathin flat lenses and axicons at telecom wavelengths based on plasmonic metasurfaces, Nano Lett. **12**, 4932 (2012).

[36] N. Yu, F. Aieta, P. Geneve, M. A. Kats, Z. Gaburro, F. Capasso, and A. Broadband, Background-free quarter-wave plate based on plasmonic metasurfaces, Nano Lett. **12**, 6328 (2012).

[37] Y. Zhao and A. Alu, Tailoring the dispersion of plasmonic nanorods to realize broadband optical meta-waveplates, Nano Lett. **13**, 1086 (2013).

[38] W. Cao, X. Yang, and J. Gao, Broadband polarization conversion with anisotropic plasmonic metasurfaces, Sci. Rep. **7**, 8841 (2017).

[39] H. Yang, G. Li, X. Su, G. Cao, Z. Zhao, F. Yu, X. Chen, and W. Lu, Annihilating optical angular momentum and realizing a meta-waveplate with anomalous functionalities, Opt. Express **25**, 16907 (2017).

[40] X. Ni, A. V. Kildishev, and V. M. Shalaev, Metasurface holograms for visible light, Nat. Commun. **4**, 2807 (2013).

[41] L. Huang, X. Chen, H. Mühlenbernd, H. Zhang, S. Chen, B. Bai, Q. Tan, G. Jin, K. Cheah, C. Qiu, J. Li, T. Zentgraf, and S. Zhang, Three-dimensional optical holography using a plasmonic metasurface, Nat. Commun. **4**, 2808 (2013).

[42] W. Wan, J. Gao, and X. Yang, Metasurface holograms for holographic imaging, Adv. Opt. Mater. **5**, 1700541 (2017).

[43] W. Wan, J. Gao, and X. Yang, Full-color plasmonic metasurface holograms, ACS Nano **10**, 10671 (2016).

[44] G. Zheng, H. Mühlenbernd, M. Kenney, G. Li, T. Zentgraf, and S. Zhang, Metasurface holograms reaching 80% efficiency, Nat. Nanotechnol. **10**, 308 (2015).

[45] N. F. Yu, P. Genevet, M. A. Kats, F. Aieta, J. P. Tetienne, F. Capasso, and Z. Gaburro, Light propagation with phase discontinuities: generalized laws of reflection and refraction, Science **334**, 333 (2011).

[46] F. Yue, D. Wen, C. Zhang, B. D. Gerardot, W. Wang, S. Zhang, and X. Chen, Multichannel polarization-controllable superpositions of orbital angular momentum states, Adv. Mater. **29**, 1603838 (2017).

[47] H. Yu, Z. Zhou, Y. Qi, X. Zhang, and Q. H. Wei, Pancharatnam–Berry optical lenses, J. Opt. Soc. Am. B **36**, D107 (2019).

[48] M. Jiang, H. Yu, X. Feng, Y. Guo, I. Chaganava, T. Turiv, O. D. Lavrentovich, and Q. H. Wei, Liquid crystal Pancharatnam-Berry micro-optical elements for laser beam shaping, Adv. Opt. Mater. **6**, 1800961 (2018).

[49] M. Jiang, Y. Guo, H. Yu, Z. Zhou, T. Turiv, O. D. Lavrentovich, and Q. H. Wei, Low f-number diffraction-limited Pancharatnam–Berry microlenses enabled by plasmonic photopatterning of liquid crystal polymers, Adv. Mater. **31**, 1808028 (2019).

[50] E. T. Whittaker, On the partial differential equations of mathematical physics, Math. Ann. **57**, 333 (1903).

[51] J. C. Gutiérrez-Vega, M. D. Iturbe-Castillo, and S. Chávez-Cerda, Alternative formulation for invariant optical fields: Mathieu beams, Opt. Lett. **25**, 1493 (2000).

[52] M. A. Bandres, J. C. Gutiérrez-Vega, and S. Chávez-Cerda, Parabolic nondiffracting optical wave fields, Opt. Lett. **29**, 44 (2004).

[53] S. Fu, T. Wang, and C. Gao, Perfect optical vortex array with controllable diffraction order and topological charge, J. Opt. Soc. Am. A **33**, 1836 (2016).